Experimental investigation of three-dimensional motion characteristics of centimeter-sized particles settling in still water

Ri Zhang,[1,*] Lun Sun,[1] Zhongwei Zhou,[1,2] Yong Liu,[1] and Domenico D. Meringolo[3]
[1]*College of Engineering, Ocean University of China, Qingdao 266100, China*
[2]*National Engineering Research Center of Dredging, Shanghai 201314, China*
[3]*Dipartimento DICEAM, Università degli Studi Mediterranea di Reggio Calabria, Via Salita Melissari, Reggio Calabria 89124, Italy*

(Received 23 October 2025; accepted 7 May 2026; published 8 June 2026)

This study experimentally investigates the three-dimensional settling process of centimeter-sized spherical particles in still water using convergent binocular vision technology. The results reveal that the number of settling particles significantly influences the settling behavior when particles are released side by side. Individual particles initially settle along nearly straight paths before randomly deflecting and returning after reaching maximum deviation points. In contrast, twin particles settle synchronously in an almost mirror-image manner, with random deflection largely suppressed—a phenomenon referred to as the mutual support phenomenon (MSP) is this study. The outermost two particles in triplet and quadruplet configurations also exhibit a typical MSP during the settling process. However, the middle particle in the triplet configuration behaves similarly to an individual particle, while the middle two particles in the quadruplet configuration display more complicated settling trajectories due to asymmetric influences from neighboring particles. Additionally, particle image velocimetry measurements are conducted in specific cases to explore the possible mechanisms underlying the random deflection of individual particles and the MSP observed in twin particles.

DOI: 10.1103/ydfl-52yk

I. INTRODUCTION

In the context of a planned seabed mining project, vertical hydraulic transport (VHT) is considered the most promising method for transporting seabed polymetallic nodules. These nodule particles, typically ranging in size from 10 to 50 mm, exhibit densities of approximately 1200 to 3000 $\mathrm{kg/m^3}$ owing to variations in porosity, resulting in a density ratio relative to seawater of about 1.14 to 2.85 [1,2]. During VHT, the nodule particles move upward due to the slip velocity between the particles and the pumped seawater. Theoretically, the minimum slip velocity should equal the terminal settling velocity of the particles in still water. Under terminal settling conditions, the particle Reynolds number (Re_p) for nodule particles is estimated to be in the range of 10^3 to 10^4. At such high Reynolds numbers, the turbulent flow field surrounding the particles has a complex influence on their motion. Therefore, studying the settling process of centimeter-sized particles in still water will help deepen our understanding of the VHT of seabed nodule particles.

There are two main concerns regarding the settling of individual particles. The first research focus is the analysis of the drag force on a single particle or its terminal settling velocity when it reaches an equilibrium settling state. Kurose and Komori [3] found that the drag force increases with higher fluid shear and rotation speed based on their three-dimensional (3D) numerical simulations.

*Contact author: zhangri@ouc.edu.cn

Brown and Lawler [4] proposed two correlations for sphere terminal velocity: one applicable for $\mathrm{Re}_p < 200\,000$, and another for more accurate predictions for $\mathrm{Re}_p < 4000$. Zhou and Cheng [5] experimentally observed that the terminal settling velocity of particles in turbulence generated by an oscillating grid is lower than that in still water. Good *et al.* [6] observed the same phenomenon and attributed the reduction in settling velocity to nonlinear drag effects. Shahi and Kuru [7] proposed an empirical correlation for the terminal velocity of a spherical particle in power-law fluids with variable viscosity and density.

The second research focus is on the complex trajectories of individual particles settling in fluid, similar to the present work. Direct numerical simulation (DNS) results by Feng *et al.* [8] revealed five different particle motion regimes: steady motion with overshoot, steady motion without overshoot, weak oscillation, strong oscillation, and irregular oscillation. Gheissary and Van Den Brule [9] found that particle settling in non-Newtonian fluid is influenced by the fluid's rheological properties and nonhomogeneous microstructure. Jenny *et al.* [10] numerically studied the settling and rising of spheres in a Newtonian fluid, identifying four regimes: steady and oblique, oblique and oscillating, zigzagging, and chaotic. These numerical results were verified by experiments conducted by Veldhuis and Biesheuvel [11]. Horowitz and Williamson [12] identified three modes of vortex shedding during particle settling: the single-sided chain of vortex rings, the double-sided chain of vortex rings, and four vortex rings.

For the freely settling twin particles, the complex flow field around the two particles causes them to either approach or move away from each other. The most famous phenomenon involving twin spheres settling is drafting-kissing-tumbling (DKT) behavior discovered by Fortes *et al.* [13], which has been systematically studied by subsequent researchers. Feng *et al.* [8] believed that DKT is controlled by lubrication, rotational couples on the long body, and wake interaction. Doostmohammadi and Ardekani [14] found that in linearly stratified fluids, DKT behavior is replaced by drafting-kissing-separation or drafting-separation phenomena. Dash and Lee [15] argued through numerical analysis that tumbling behavior is caused by repulsive hydrodynamic forces originating from the vertical and lateral migrations of the spheres. Liao *et al.* [16] found that when a small sphere is placed below a large one, the kissing duration decreased with increasing diameter ratio. Tsai *et al.* [17] pointed out that due to wall effects, the two spheres can form a chain instead of separating.

Another widely studied case is the settling of twin spheres side by side. Joseph *et al.* [18] observed that when the initial distance is small, two spheres attract, contact, and interlock with each other in a viscoelastic fluid. Wu and Manasseh [19] found that when $\mathrm{Re}_p > 0.1$, particles repel each other, and the separation displacement depends on Re_p in a Newtonian fluid. Cao *et al.* [20] concluded that as the line between the initial centers of the two spheres shifts from horizontal to vertical, the interaction evolves from repulsion to attraction. Nie and Lin [21] used the lattice Boltzmann method (LBM) to simulate the sedimentation of two equal-sized spheres with different densities. At low Galileo number (Ga), the motion reaches a steady state for small density differences and a periodic state for large ones. At high Ga, the spheres tend to oscillate. Chu *et al.* [22] demonstrated that the fluid pressure in the gap region is lower than outside the gap, causing the spheres to move toward each other as they fall. Then, vortices alternately shed behind the spheres, generating lateral forces that deviate the spheres from the vertical trajectory. Liu *et al.* [23] showed that the release method significantly affects the settling of two spheres. Chiu *et al.* [24] revealed that wakes dominate the fluid-sphere interaction. The pressure difference caused by velocity differences pulls the spheres toward each other, and the two proximate spheres generate a united wake that blocks the inner-side flow, pushing them apart. The experimental results of Xiao *et al.* [25] revealed that the initial gap between twin spheres and Re_p are the most important factors affecting the settling process. However, most of these studies focused on the two-dimensional (2D) motion of twin particles.

Some studies on the settling process of multiple particles or granular systems focus on granular settling velocity or particle clustering, which is a research hotspot in the field of sediment dynamics. Di Felice [26] found that the settling velocity of dilute suspensions of equal-sized spheres is a linear function of the particle volume concentration. Daniel *et al.* [27] observed that the mean square of cluster size grows as the 2/3 power of time due to isotropic repulsive forces between particles. Chou *et al.* [28] developed a two-way coupled Euler-Lagrange model to simulate the suspension of fine particles in liquid flows, which retained the particle information at each time step without requiring Lagrangian particle tracking. Shahi and Kuru [29] proposed an empirical model for the settling velocity of quartz sands in water based on a dimensionless diameter and Re_p. Zhang *et al.* [30] applied an improved multilayer extraction sampling method to investigate the settling velocity of soil particles in dredged slurry. Petersen *et al.* [31] observed that the settling velocity of sub-Kolmogorov inertial particles in homogeneous turbulence can be several times larger than the still-air terminal velocity, caused by downward fluid fluctuations that preferentially sweep the particles.

Other studies examine the influence of particle-particle interactions on the morphology of particle groups during settling, which is more related to the present study. Patankar *et al.* [32] presented a Lagrange-multiplier-based fictitious-domain method for particulate flow and found that particles settling in a viscoelastic fluid tend to form chains. Feng and Michaelides [33] used the LBM to analyze the settling of 504 particles, showing that two eddies form and grow at the sides of the container. Yacoubi *et al.* [34] investigated the dynamics of horizontal arrays of settling spheres using DNS. They found that for odd-numbered arrays, the middle sphere always leads, whereas for even-numbered arrays, the steady-state shape is concave down. Nie *et al.* [35] used the LBM to simulate the sedimentation of eight spheres at $\mathrm{Re}_p \approx 250$. As the initial gap increased, the configurations evolved successively from concave-down to "M" shaped, and finally to in-line arrangements. However, these studies were conducted via numerical simulations.

Currently, few studies have examined how particle number affects the settling behavior of centimeter-sized particles, which represent the typical size range of seabed mineral particles. Furthermore, most investigations on the settling of twin particles have focused on 2D motion, and studies involving multiple particles have primarily relied on numerical simulations. To address this gap, the present work experimentally investigates the 3D settling process of centimeter-scale particles in different numbers using a convergent binocular vision (CBV). Additionally, particle image velocimetry (PIV) is employed to elucidate the mechanisms by which particle number affects the settling behavior.

II. EXPERIMENTAL SETUP

The present experimental study is divided into two main parts. In experiment I, the 3D settling processes of centimeter-sized particles in still water are captured using a CBV technology. The effects of particle number, particle size, and initial interparticle gap on the settling behavior are systematically examined. In experiment II, PIV is applied to measure the flow field surrounding individual and twin particles under selected representative conditions.

A. Experimental apparatus and layout

The experimental setup for experiment I is shown in Fig. 1(a), comprising two high-speed cameras, two light-emitting diode (LED) lamps, a release device, a transparent water tank ($0.6\times0.4\times0.8$ m^3), and test spheres. The high-speed cameras are arranged along the x and y directions of the tank to capture the 3D free settling processes of particles. The two LED lamps are positioned on opposite sides of the tank, corresponding to the camera orientations. The tank is constructed of transparent plexiglass to ensure high optical clarity, and light diffuser plates are installed on the light-facing sides along the x and y directions to achieve uniform illumination within the flow field.

For experiment II, the high-speed camera along the x direction, the two LED lamps, and the diffuser plates are removed. Instead, two laser sources are positioned on the positive-x side of the tank, with one directed upward at an angle of 30° and the other directed downward at 60°. A mirror is placed on the negative-x side of the tank to reflect the laser beams. The alignment of the laser sources

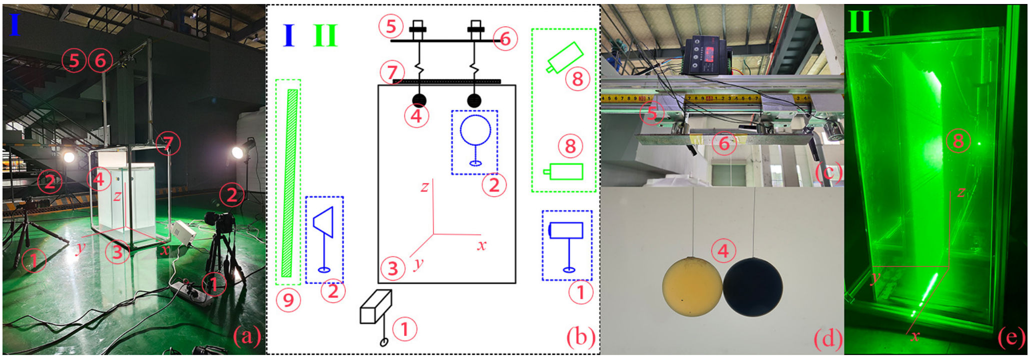

FIG. 1. Experimental devices and layout: (a) layout for experiment I; (b) schematic diagram, where the devices in the blue and green boxes are used for experiments I and II, respectively; (c) release device; (d) test spheres; (e) laser-illuminated observation plane in experiment II. Labels: ① high-speed cameras, ② LED lamps for experiment I, ③ tank, ④ test spheres, ⑤ electromagnet and demagnetizer, ⑥ perforation steel bar, ⑦ buffer rubber pad, ⑧ laser sources for experiment II, and ⑨ mirror for experiment II.

and the mirror is carefully adjusted so that the incident and reflected laser beams coincide on the same plane, ensuring that the illuminated observation plane is unobstructed by the test particles and minimizing shadowing effects. The laser-illuminated observation plane in experiment II is shown in Fig. 1(e).

The high-speed cameras used in the experiments are Revealer M230, featuring a full-frame acquisition speed of 3000 frames per second (fps) and a maximum resolution of 1920×1080 pixels. For experiment I, the frame rate and resolution are set to 1500 fps and 1280×1080 pixels, respectively. Each camera is focused on the center of the tank. The images are processed using the Revealer high-speed image analysis system, which provides a measurement accuracy of 0.01 pixels and is used to capture the 2D coordinates of the particle in each frame during the settling process. The LED lamps (Jinbei EF-220) are set to an output power of 220 W and a color temperature of 6500 K. These bright illumination conditions ensure high-quality imaging during each filming session.

For experiment II, only the camera facing the observation plane is retained, and its maximum performance settings are enabled. The laser sources used in the experiments are GL-LS-18, which stably emitted a continuous 532-nm laser sheet, illuminating a flow field with a thickness of approximately 2 mm. Particle images were recorded by a high-speed camera at 1500 fps, corresponding to a time interval of 666.7 μs between consecutive frames. The PIV velocity fields were obtained by analyzing pairs of consecutive images. The tracer particles used in the PIV measurements are made of polystyrene, with a density of $1.03\ \mathrm{g/cm^3}$ and a mean diameter of 50 μm. During the PIV experiments, an opaque curtain is used to enclose the laser sources, mirror, camera, and tank, thereby enhancing the clarity and contrast of the laser-illuminated observation plane.

The test spheres [Fig. 1(d)] are made of plexiglass with a density of $1254.7\pm0.5\ \mathrm{kg/m^3}$. Their diameters are 29.985 ± 0.005 mm, 39.978 ± 0.004 mm, and 49.985 ± 0.008 mm. Based on the terminal settling velocity, the corresponding Stokes numbers St_p are approximately 817, 1244, and 1611, respectively, while the corresponding Re_p are approximately 14 700, 22 400, and 29 000, respectively. For the multiple-particle tests, it is crucial to ensure that all test spheres are released into the water simultaneously and without any initial velocity. To achieve this, a custom release device is designed and produced [Fig. 1(c)]. Each test sphere is attached to a 1-m lightweight thread using glue. The thread has a density of 52.0 ± 0.4 mg/m and a diameter of 0.18 ± 0.01-mm. The other end of the thread is secured to a specially designed steel bar with laser-cut perforations spaced at 1 cm intervals to guide the threads. Before each test, the steel bar connected to the threads is held in place by an electromagnet while the test spheres are submerged underwater. Once the electromagnet is powered off, a demagnetizer immediately neutralizes the magnetic force, allowing the steel bar to

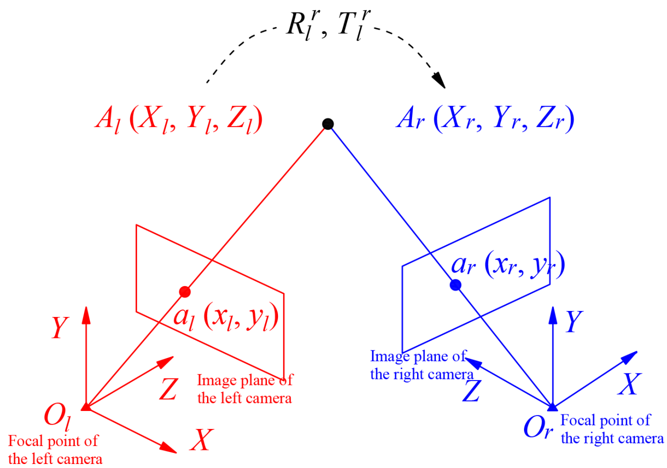

FIG. 2. Basic principle of convergent binocular vision (CBV).

fall freely through the air and land on a buffer rubber pad positioned above the tank. Due to water resistance, the test spheres descend more slowly than the steel bar, causing the threads to slacken and thus minimizing their influence on the settling process.

Comparative tests with individual particles, both with and without the attached threads, confirm that the glued threads have a negligible impact on the motion behavior of the test spheres. Details of these comparative tests are presented in the Appendix. Additionally, our previous study [36] systematically investigated the influence of wall effects on the settling process of particles with diameters of 30, 40, and 50 mm. The results showed that when the distance between the wall and the particle center exceeds twice the particle diameter, the wall effect on the settling process can be neglected for all three particle sizes. In the present work, the distance between the outermost particles and the tank wall in each test remains much larger than twice the particle diameter, even when these particles reach their maximum deflection amplitude. Therefore, the influence of the wall on the particle settling process can be neglected.

B. Convergent binocular vision

The two sets of 2D coordinates of the particle obtained from the synchronized images captured by the two cameras from intersecting perspectives are converted into 3D coordinates using the CBV method. The basic principle of CBV is illustrated in Fig. 2. The left camera projects the 3D particle coordinates $A_l\ (X_l,\ Y_l,\ Z_l)$ onto the 2D pixel coordinates $a_l(x_l,\ y_l)$ on the image plane, using the following transformation matrix:

$$Z_l \begin{bmatrix} x_l \\ y_l \\ 1 \end{bmatrix} = \begin{bmatrix} f_{lx} & 0 & u_{0l} \\ 0 & f_{ly} & v_{0l} \\ 0 & 0 & 1 \end{bmatrix} \begin{bmatrix} X_l \\ Y_l \\ Z_l \end{bmatrix}. \tag{1}$$

Similarly, the transformation relationship between the 3D particle coordinates $A_r(X_r,\ Y_r,\ Z_r)$ and the 2D pixel coordinates $a_r\ (x_r,\ y_r)$ captured by the right camera is

$$Z_r \begin{bmatrix} x_r \\ y_r \\ 1 \end{bmatrix} = \begin{bmatrix} f_{rx} & 0 & u_{0r} \\ 0 & f_{ry} & v_{0r} \\ 0 & 0 & 1 \end{bmatrix} \begin{bmatrix} X_r \\ Y_r \\ Z_r \end{bmatrix}, \tag{2}$$

where f_{lx}, f_{ly}, f_{rx}, and f_{ry} represent the focal length, and $(u_{0l},\ v_{0l})$ and $(u_{0r},\ v_{0r})$ are the origin point coordinates of the left and right image planes, respectively. The left and right cameras establish coordinate systems with their respective focal points as the origins, and $(X_l,\ Y_l,\ Z_l)$ and $(X_r,\ Y_r,\ Z_r)$

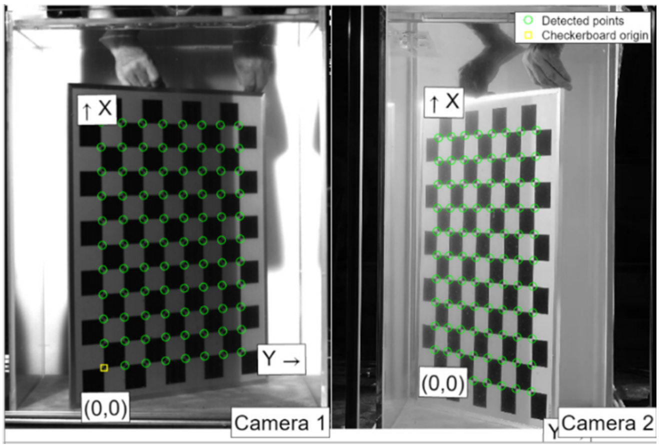

FIG. 3. Checkerboard calibration for convergent binocular cameras.

represent the 3D coordinates of the particle in the left and right coordinate systems, respectively. The transformation relationship between the 3D coordinates captured by the two cameras is

$$\begin{bmatrix} X_r \\ Y_r \\ Z_r \\ 1 \end{bmatrix} = \begin{bmatrix} R_l^r & T_l^r \\ 0 & 1 \end{bmatrix} \begin{bmatrix} X_l \\ Y_l \\ Z_l \\ 1 \end{bmatrix} = \begin{bmatrix} r_{11} & r_{12} & r_{13} & t_1 \\ r_{21} & r_{22} & r_{23} & t_2 \\ r_{31} & r_{32} & r_{33} & t_3 \\ 0 & 0 & 0 & 1 \end{bmatrix} \begin{bmatrix} X_l \\ Y_l \\ Z_l \\ 1 \end{bmatrix}, \tag{3}$$

where R_l^r is the rotation matrix of the right coordinate system relative to the left coordinate system, and T_l^r is the translation matrix.

If the 2D coordinate points $a_l\,(x_l,\ y_l)$ and $a_r(x_r,\ y_r)$ on the image planes of the left and right cameras are known, seven equations can be constructed based on matrices (1)–(3). There are 20 unknowns, including 4 focal lengths $(f_{lx},\ f_{ly},\ f_{rx},\ f_r)$, 4 origin point coordinates $(u_{0l},\ v_{0l},\ u_{0r},\ v_{0r})$, 9 elements of rotation matrix r_{ij}, and three elements of translation matrix t_i. Theoretically, if the coordinates of 12 points captured by the two cameras are known, the 20 unknowns can be solved. In the present work, the classical chessboard calibration method of Zhang [37] is applied to determine the rotation matrix R_l^r and translation matrix T_l^r. As shown in Fig. 3, the size of the checkerboard is $650\times500\ \text{mm}^2$, covered with black and white squares of 50 mm. With the help of the Stereo Camera Calibrator toolbox in matlab, the coordinate transformation relationship between the left and right cameras is determined. The 3D coordinates of any particle can then be calculated as follows:

$$X_l = \frac{f_{ly}(u_{0l} - x_l)(f_{rx}t_1 + t_3u_{0r} - t_3x_r)}{L}, \tag{4}$$

$$Y_l = \frac{f_{lx}(v_{0l} - y_l)(f_{rx}t_1 + t_3u_{0r} - t_3x_r)}{L}, \tag{5}$$

$$Z_l = \frac{-f_{lx}f_{ly}(f_{rx}t_1 + t_3u_{0r} - t_3x_r)}{L}, \tag{6}$$

$$L = \begin{pmatrix} f_{lx}f_{ly}f_{rx}r_{13} + f_{lx}f_{ly}r_{33}u_{0r} - f_{ly}f_{rx}r_{11}u_{0l} - f_{lx}f_{rx}r_{12}v_{0l} + f_{ly}f_{rx}r_{11}x_l \\ -f_{lx}f_{ly}r_{33}x_r + f_{lx}f_{rx}r_{12}y_l - f_{ly}r_{31}u_{0l}u_{0r} - f_{lx}r_{32}u_{0r}v_{0l} + f_{ly}r_{31}u_{0r}x_l \\ +f_{ly}r_{31}u_{0l}x_r + f_{lx}r_{32}u_{0r}y_l + f_{lx}r_{32}v_{0l}x_r - f_{ly}r_{31}x_lx_r - f_{lx}r_{32}x_ry_l \end{pmatrix}. \tag{7}$$

TABLE I. Experimental cases.

Test configuration	Case	No. of tests
Individual spherical particles	1s.30.0.00D, 1s.40.0.00D, 1s.50.0.00D	
	2s.30.1.67D, 2s.30.2.00D, 2s.30.2.33D	
Twin spherical particles	2s.40.1.50D, 2s.40.1.75D, 2s.40.2.00D	
	2s.50.1.60D, 2s.50.1.80D, 2s.50.2.00D	30
Triplet spherical particles	3s.40.1.75D, 3s.40.2.00D, 3s.40.2.25D	
Quadruplet spherical particles	4s.40.2.00D, 4s.40.2.25D, 4s.40.2.50D	

III. MOTION ANALYSIS OF THE SETTLING PROCESS

The 3D settling processes of the individual, twin, triplet, and quadruplet spherical particle configurations were observed over time. Each test was repeated 30 times to obtain statistically reliable results for the particle motion characteristics, resulting in a total of 540 tests conducted. All experiments are conducted at a controlled temperature of 25 °C, ensuring minimal variation in fluid viscosity over time. A resting interval of 20 min is maintained between experiments to allow the water to return to a quiescent state.

Each experimental case is designated as "*A*s.*B*.*C*D," where *A* represents the number of particles, *B* denotes the particle diameter (in millimeters), and *C* denotes the initial release gap normalized by the particle diameter. For cases involving three particles, the particles are labeled as "L" (left), "M" (middle), and "R" (right). For cases involving four particles, the particles are labeled as "L" (left), "ML" (middle left), "MR" (middle right), and "R" (right), from left to right. All experimental cases are summarized in Table I.

A. Settling process of individual particles

To enhance clarity, Fig. 4(a) presents the partial 3D settling trajectories of individual particles with a size of 40 mm. The particle trajectories transition from nearly straight-line motion to random

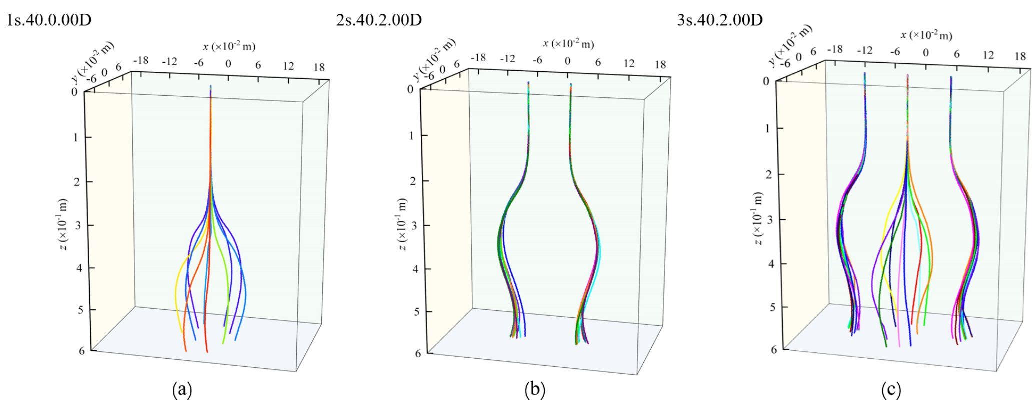

FIG. 4. 3D settling trajectories of 40-mm particles: (a) individual particles, (b) two particles, (c) three particles.

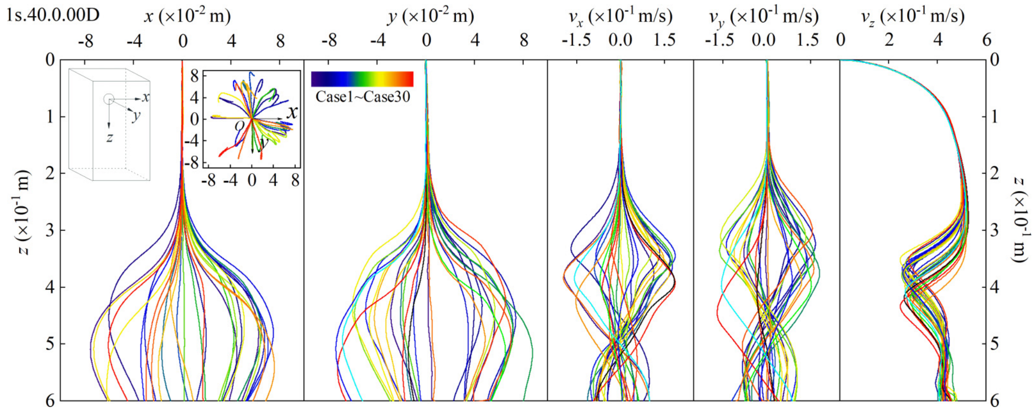

FIG. 5. Three-view image of settling trajectories and velocities of individual particles with a size of 40 mm from 30 experiments.

deflection. Once the deflection reaches its maximum amplitude, the trajectories shift toward the side opposite to the initial motion direction.

1. Settling trajectories of individual particles

The three-view image of 30 trajectories of individual particles with a size of 40 mm is provided in Fig. 5. In the initial stage, the settling particles move approximately along straight paths, with the 30 measured particle trajectories almost overlapping. When the vertical particle displacement z reaches approximately 0.2 m, the particles begin to deflect from their previously straight paths. The deflection directions are highly random, and almost no two trajectories completely overlap. The projection of the trajectories onto the x-y plane shows that the deflection angles are approximately uniformly distributed between 0 and 2π. Furthermore, the trajectory profiles on the x-z and y-z planes are quite similar, indirectly indicating an equal probability of particle deflection in various directions.

Although the particle deflection is random, the deflected particles are observed to predominantly move near a specific plane. This plane passes through the z axis and the maximum deflection point and is referred to as the x'-z plane in the present study. The maximum deflection point is the point farthest from the release position when projected onto the x-y plane. In addition, the deflected particles exhibit fluctuations perpendicular to the x'-z plane. Hence, the plane perpendicular to the deflection plane is defined as the fluctuation plane, referred to as the y'-z plane. Decomposing the motion of individual particles into components on the deflection plane x'-z and the fluctuation plane y'-z provides a clearer description of particle motion, as shown in Fig. 6. The 30 particle trajectories exhibit similar motion characteristics. On the deflection plane x'-z, the 40-mm particles gradually deviate from vertical motion, move toward the maximum deflection point, and then reverse direction. On the fluctuation plane y'-z, the particles fluctuate around the z axis.

The mean particle trajectories obtained from 30 experiments are shown in Fig. 7, where the displacement and velocity are respectively normalized as

$$U^* = \frac{\rho_p v_p D}{\mu}, \tag{8}$$

$$x^* = \frac{x}{D}, \tag{9}$$

$$y^* = \frac{y}{D}, \tag{10}$$

$$z^* = \frac{z}{D}, \tag{11}$$

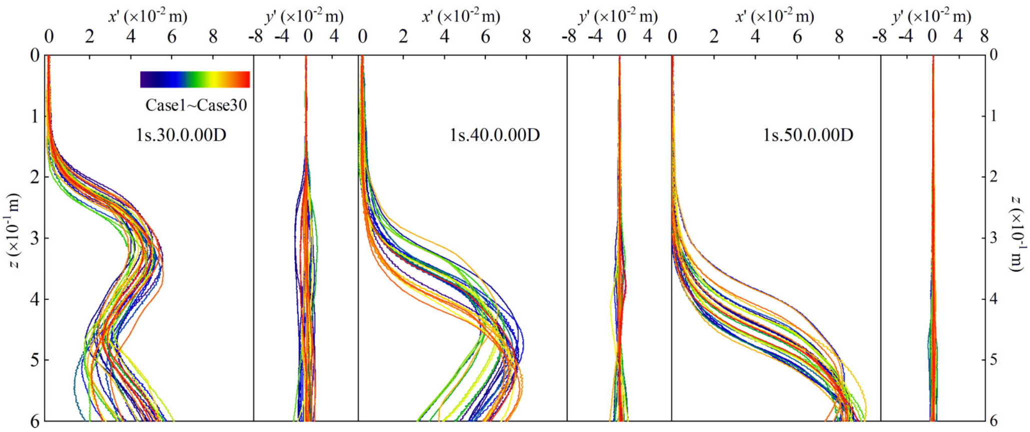

FIG. 6. Settling trajectories of individual particles on the deflection and fluctuation planes from 30 experiments.

where ρ_p is the particle density, v_p is the particle velocity, D represents the particle diameter, and μ is the dynamic viscosity of water. The figure clearly reveals the characteristics of particle motion on both the deflection and fluctuation planes. The mean particle displacement $\bar{y}'^*$ is close to zero on the fluctuation plane. Horizontal error bars are included in the mean trajectories, where the length of each bar represents the standard deviation of the lateral displacement at the corresponding settling position, illustrating the possible range of particle positions during the settling process. Generally, the standard deviation of x'^* is significantly larger than that of y'^*, indicating that random particle fluctuation is more intense on the deflection plane x'-z.

As shown in Fig. 6, the settling movement of the 30- and 50-mm particles are similar to those of the 40-mm particles and can also be decomposed into motions on the deflection and fluctuation planes. On the deflection plane x'-z, larger particles exhibit a longer vertical displacement z before deflection occurs. On the fluctuation plane y'-z, although the mean displacement $\bar{y}'^*$ for all particle sizes remains close to zero, an increase in particle size leads to a smaller fluctuation amplitude, as indicated by the error bars. The motion characteristics on the deflection and fluctuation planes indicate that larger particles possess greater inertia and therefore respond more slowly to disturbances from the surrounding flow field.

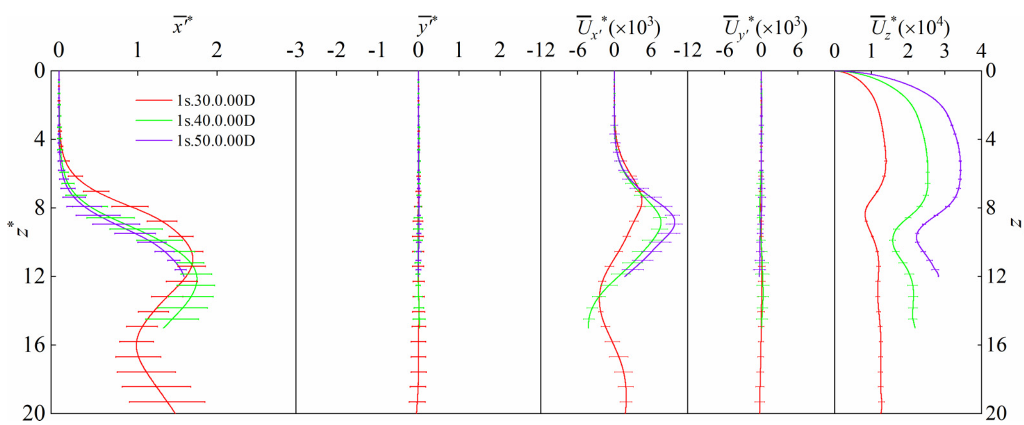

FIG. 7. Mean settling trajectory and velocity of individual particles on the deflection and fluctuation planes.

2. Settling velocities of individual particles

The settling velocities of 40-mm particles in 30 tests are shown in Fig. 5. The profiles of v_x and v_y are quite similar, further demonstrating the isotropy of the random particle deflection. The mean dimensionless settling velocities on the deflection and fluctuation planes, shown in Fig. 7, more clearly illustrate the particle settling characteristics. In the initial settling process, the mean deflection velocity $\bar{U}^*_{x'}$ is almost negligible. As the mean vertical velocity $\bar{U}^*_z$ increases sharply, particles begin to deflect, and $\bar{U}^*_{x'}$ appears and continuously increases to a peak value before decreasing. When the particle reaches the maximum deflection point, the mean deflection velocity $\bar{U}^*_{x'}$ decreases to zero.

The mean vertical velocity $\bar{U}^*_z$ sharply increases to a peak value, enters a plateau region, then suddenly decreases ("squat") and subsequently recovers to a relatively stable velocity slightly lower than the peak value. This "squat" occurs after the mean deflection velocity $\bar{U}^*_{x'}$ reaches its peak. As the mean deflection velocity $\bar{U}^*_{x'}$ decreases, the mean vertical velocity $\bar{U}^*_z$ recovers. Throughout the settling process, the mean vertical velocity $\bar{U}^*_z$ is significantly larger than the mean deflection velocity $\bar{U}^*_{x'}$, and the mean fluctuation velocity $\bar{U}^*_{y'}$ remains nearly zero.

The mean deflection velocity $\bar{U}^*_{x'}$ of particles with different sizes exhibits a sinelike variation. Since the deflection velocity $\bar{U}^*_{x'}$ is normalized in a manner similar to the Reynolds number Re_p and is positively correlated with inertial forces, larger particles exhibit higher peak values. The mean vertical velocity $\bar{U}^*_z$ shows a similar trend across different particle sizes: a sharp increase to a peak, followed by a plateau, a squat, and a subsequent recovery. As the particle size increases, the variation magnitude of the velocity $\bar{U}^*_z$ becomes larger, which can again be attributed to the greater inertia of larger particles. Since the vertical velocity v_z is significantly greater than the lateral velocities v_x and v_y, the dimensionless velocity $\bar{U}^*_z$ defined based on the vertical velocity v_z is approximately equal to the particle Reynolds number Re_p during particle settling. Therefore, the trend of $\bar{U}^*_z$ reflects the variation of Re_p.

The length of the error bars along the velocity curves represents the intensity of velocity fluctuations. Two main observations can be made: (1) smaller particles exhibit higher peak velocity fluctuations on both the deflection and fluctuation planes, and (2) velocity fluctuations on the deflection plane x'-z are generally greater than those on the fluctuation plane y'-z, consistent with the displacement characteristics.

3. Possible reason for random deflection

As shown in Fig. 6, although the deflection angles are highly random, the projections of 30 particle trajectories on the deflection and fluctuation planes remain quite similar. In the present work, the flow field evolution on the deflection plane of an individual settling 40-mm particle is examined using PIV measurements. Since individual particles deflect randomly during settling, multiple attempts were required to align the actual deflection plane with the preset laser sheet. The flow field at different instants during the settling process is presented in Fig. 8. Herein, x denotes the particle deflection direction and z denotes the falling direction.

During the initial vertical descent, the flow field around the spherical particle is regular and axisymmetric. The velocity vectors originate from the particle's bottom surface, move along both sides, and converge at the top center, as illustrated in Figs. 8(a) and 8(b). However, this symmetric bottom-to-top wake structure is inherently unstable. As the particle's settling velocity increases, the convergence point (marked by a red "X" enclosed in white dashed lines in Fig. 8) above the particle begins to deviate from the top center, as if it "slides away." We infer that the transition from symmetry to asymmetry in the wake structure generates a lateral force that pushes the particle in the direction opposite to the deviation of the convergence point, as shown in Fig. 8(c).

Since the initial deviation of the convergence point is random, the direction of the particle's first deflection is also random. Once the particle deflects, the bottom-to-top flow is no longer constrained by the particle's geometry, allowing the asymmetric wake to develop into a coherent vortex. As the particle continues to settle, it gradually separates from this vortex region, leading to vortex

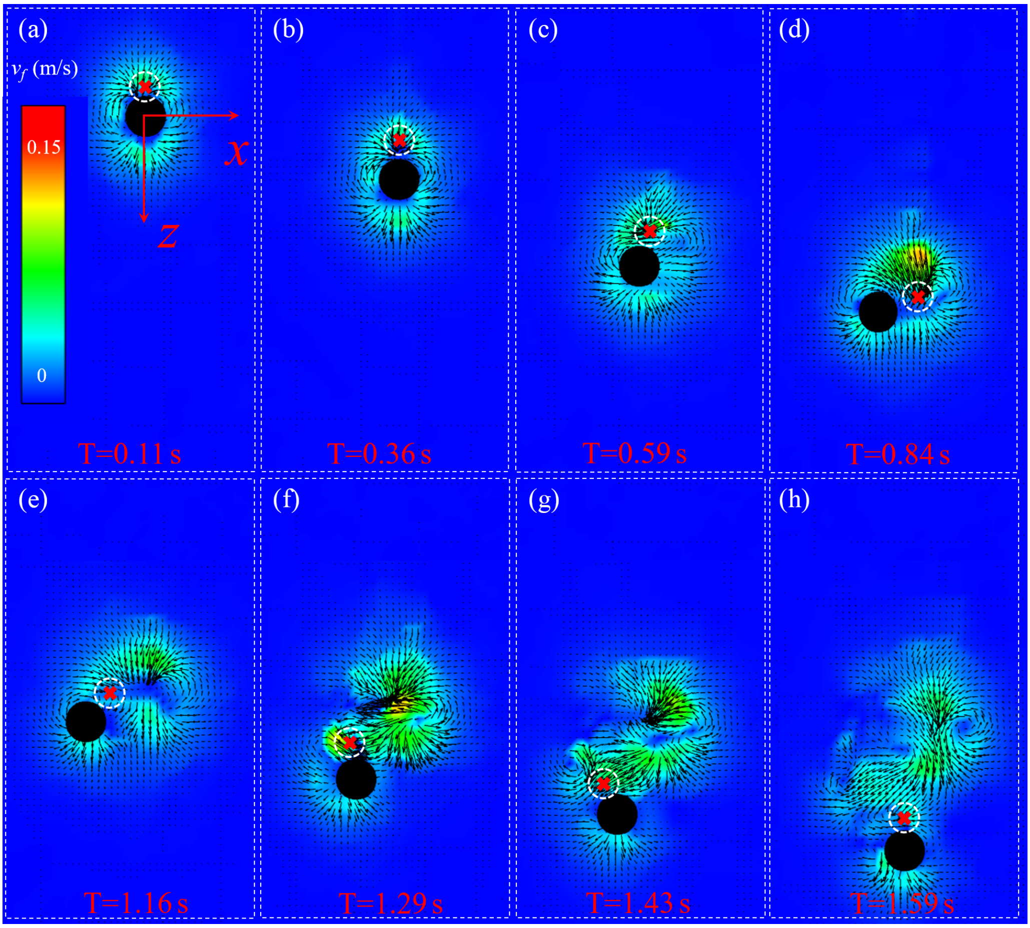

FIG. 8. Contours and vectors of the fluid velocity v_f around an individual particle with a size of 40 mm measured using PIV at different instants.

shedding, as depicted in Fig. 8(d). Subsequently, the flow reestablishes a bottom-to-top pattern in which the velocity vectors again originate from the particle's bottom surface and converge at its top, as shown in Fig. 8(e). However, this new convergence point is influenced by the residual flow of the previously shed vortex and deviates toward the side opposite the previous vortex region. This deviation induces a secondary deflection in the direction opposite to the first, with the corresponding flow field evolution illustrated in Figs. 8(f)–8(h). Notably, the occurrence of the secondary deflection is strongly correlated with the preceding vortex dynamics, suggesting a dynamic interaction between vortex shedding and the particle's lateral displacement.

In summary, the random initial deviation of the convergence point gives rise to the random direction of the particle's first deflection, while the subsequent deflection—governed by the influence of the previously shed vortex—occurs in the opposite direction. This mechanism explains why particles, despite exhibiting random initial deflections, tend to move within a nearly fixed plane during the settling process. Nevertheless, the present study acknowledges the limitation that the detailed mechanism of the lateral force generated by wake instability has not been fully resolved. Future work incorporating higher-resolution PIV measurements will be necessary to fully elucidate the mechanism underlying random particle deflection.

B. Settling process of twin particles

Figure 4(b) depicts the partial 3D settling trajectories of twin particles with a size of 40 mm. The trajectories exhibit notable symmetry, with only slight fluctuations near the initial release plane, while the random deflections observed during individual particle settling are significantly weakened. This phenomenon, wherein twin particles mutually support each other and suppress the random deflection of each particle, is designated as the mutual support phenomenon (MSP).

1. Settling trajectories of twin particles

The mean dimensionless settling trajectories and velocities of twin particles with different particle sizes and initial gaps are shown in Fig. 9. For 40-mm particles, their mean trajectories on the x-z plane are symmetrical and similar to those of individual particles settling on the deflection plane x'-z. After an initial phase of nearly vertical settling, the twin particles simultaneously deflect from their vertical paths, move away from each other, reach maximum deviation points, and then move back toward each other. After approaching, they separate again. However, compared with the settling of individual particles, the vertical movement, deflection, and return process of twin particles is accelerated. On the y-z plane, the mean displacement $\bar{y}^*$ remains nearly zero.

Twin particles released simultaneously exhibit three motion characteristics. First, the trajectories of the twin particles are nearly synchronized and mirror symmetric. The particles initially follow approximately straight paths and subsequently diverge laterally in opposite directions. After the separation reaches its maximum amplitude, the trajectories gradually converge back toward the center, exhibiting a trend of approaching each other. The larger the initial gap, the more similar the trajectories are to those of individual particles. Second, their deflection is constrained to the initial release plane. That is, the x-z plane serves as their deflection plane x'-z, and the y-z plane remains the fluctuation plane y'-z. Third, the deflection and subsequent return motion of each particle results in a cycle of separation-approach behavior. A smaller initial gap leads to a faster separation-approach cycle. These three characteristics together define the MSP observed in the present work.

As shown in Fig. 9, the mean trajectories of twin particles with sizes of 30 and 50 mm are quite similar to those of the 40-mm particles, also exhibiting the MSP. They initially settle vertically before entering a symmetrical separation-approach cycle. Similar to the behavior of individual particles, smaller particles exhibit more fully developed trajectories, while the 50-mm particles experience only a single cycle. Therefore, the trajectory of a large particle can be regarded as a local segment of that of a smaller particle.

As in Fig. 7, the lengths of error bars in Fig. 9 represent the standard deviations of the corresponding parameters. To more clearly illustrate these variations, the standard deviations of displacement and velocity are replotted in Fig. 10. Colored curves represent twin particles with different initial gaps. Solid black lines show the standard deviations of individual particles on the x-z and y-z planes, and dashed lines represent those on the x'-z and y'-z planes. On the x-z and y-z planes, the initial gap has little effect on the standard deviations. Although $\sigma(x^*)$ and $\sigma(y^*)$ differ, they are of the same order of magnitude and significantly smaller than those for individual particles, highlighting the suppression of random deflection through the MSP.

Since the deflection planes differ, comparing $\sigma(x^*)$ and $\sigma(y^*)$ of twin particles to $\sigma(x'^*)$ and $\sigma(y'^*)$ of individual particles is more meaningful. The standard deviation of displacement reflects the divergence caused by particle fluctuations. On the fluctuation plane, the standard deviations $\sigma(y^*)$ and $\sigma(y'^*)$ are similar. However, on the deflection plane, $\sigma(x'^*)$ is slightly larger than $\sigma(x^*)$, indicating that the MSP restricts both the location of the deflection plane and random particle fluctuations.

2. Settling velocities of twin paricles

As shown in Fig. 9, the mean dimensionless deflection velocities of twin particles, $\bar{U}_x^*$, on the x-z plane also display remarkable symmetry. As discussed in the previous section, the MSP

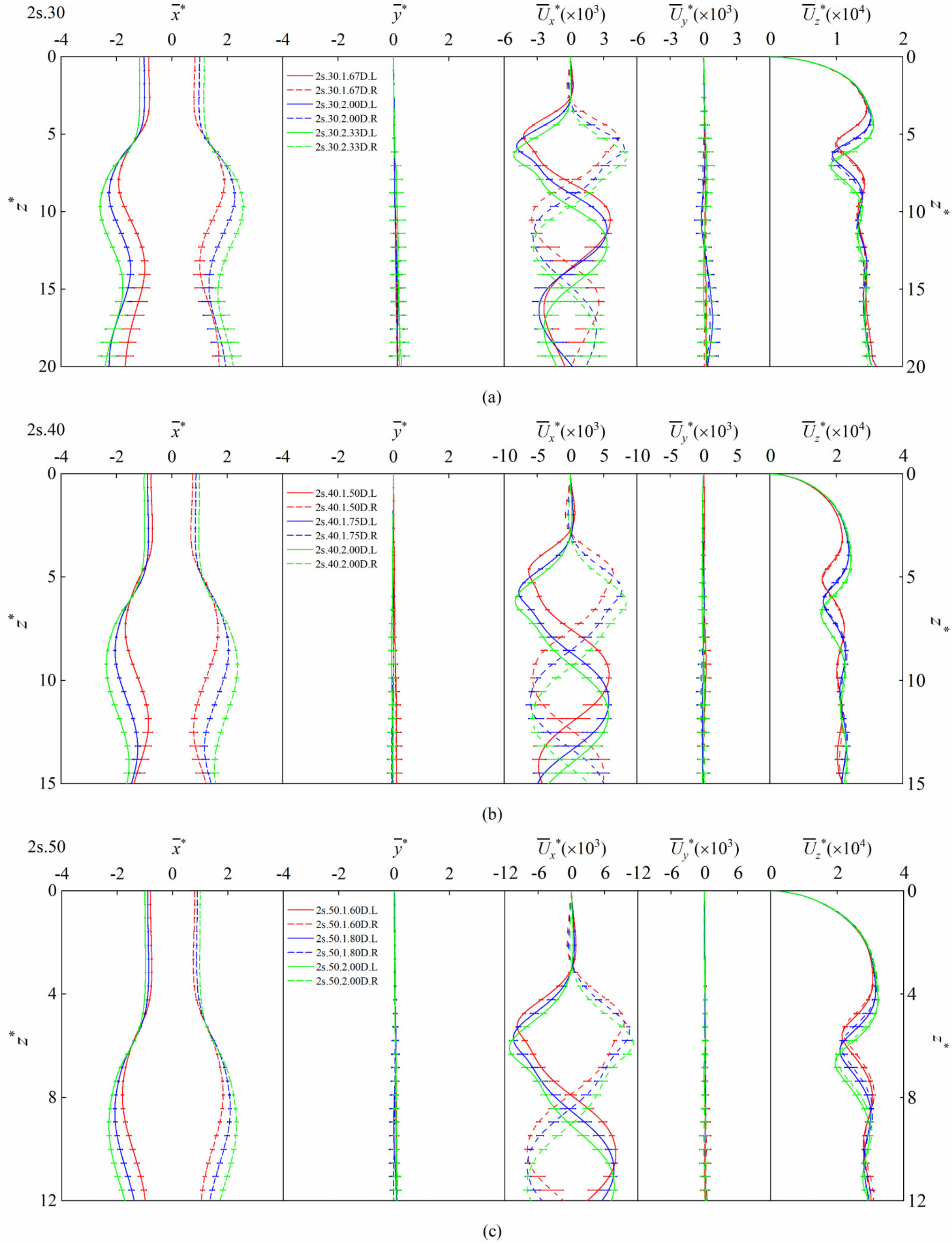

FIG. 9. Mean settling trajectory and velocity of twin particles on the *x*-*z* and *y*-*z* planes: (a) 30 mm, (b) 40 mm, and (c) 50 mm.

accelerates the separation-approach cycle. Taking 40-mm particles as an example, compared to individual particles, the $\bar{U}_x^*$ curves of twin particles are more fully developed. After a slight increase and decrease, the curves present a sinusoidal form with decaying amplitude. The periodic velocity change causes the cyclic separation-approach motion.

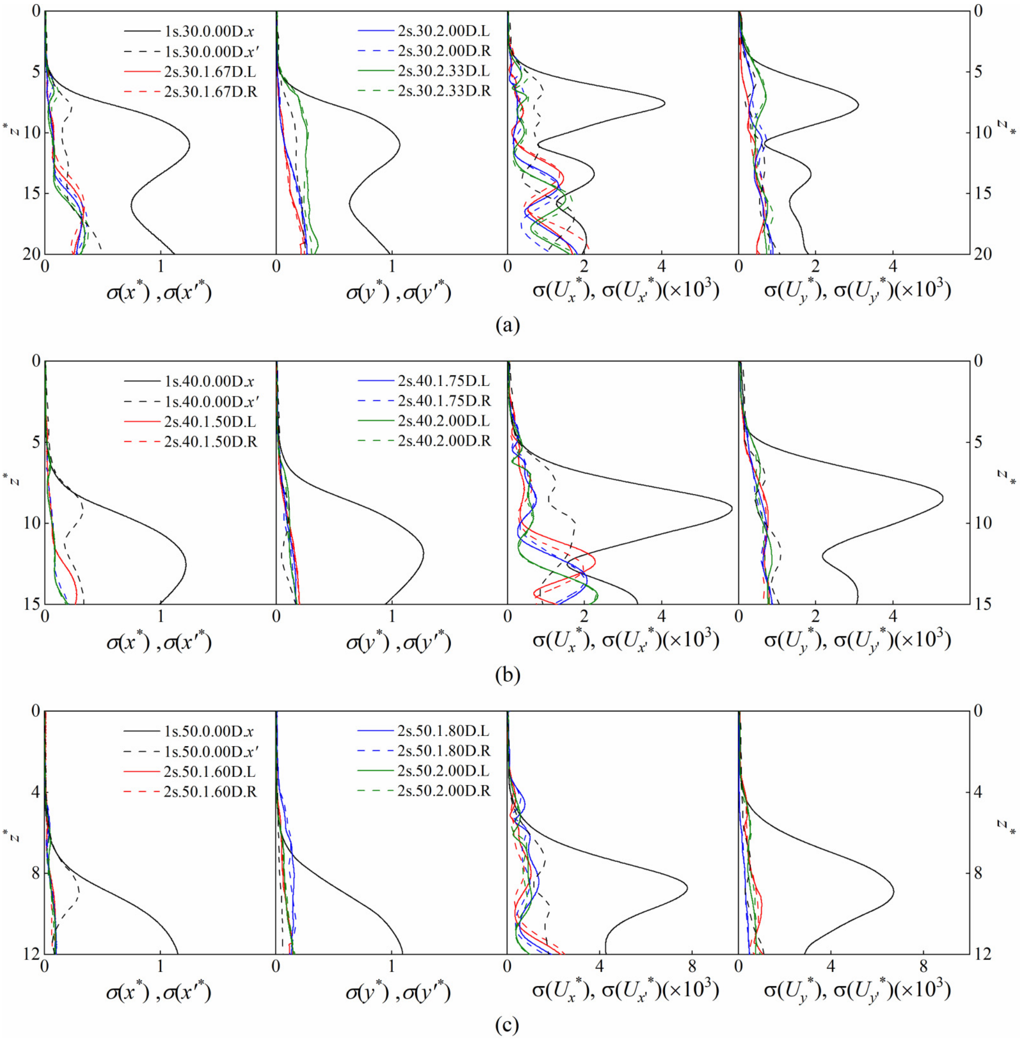

FIG. 10. Standard deviations of displacement and velocity of individual and twin settling particles on the deflection and fluctuation planes: (a) 30 mm, (b) 40 mm, and (c) 50 mm.

On the *y*-*z* plane, the mean fluctuation velocities of twin particles, $\bar{U}_y^*$, remain close to zero, indicating only random fluctuations without systematic deflection. Similar to the mean deflection velocity $\bar{U}_x^*$, the mean vertical velocity of twin particles, $\bar{U}_z^*$, is a more developed version of that of individual particles. The mean vertical velocity $\bar{U}_z^*$ rapidly rises to a peak, then exhibits a "squat" and fluctuates around a value slightly less than the peak. Notably, the maximum deflection and vertical velocities of twin particles are comparable to those of individual particles, suggesting that the MSP does not significantly impact the maximum settling velocity. Similarly, the mean vertical velocity $\bar{U}_z^*$ is approximately equal to Re_p, and hence the curve in Fig. 9 also reflects the variation of Re_p along the settling path.

As shown in Fig. 9, the effect of particle size on the settling velocity of twin particles is the same as that on individual particles. Larger particles, due to their greater inertia, are less sensitive to flow field disturbances, resulting in their deflection and vertical velocity curves being only a fraction of

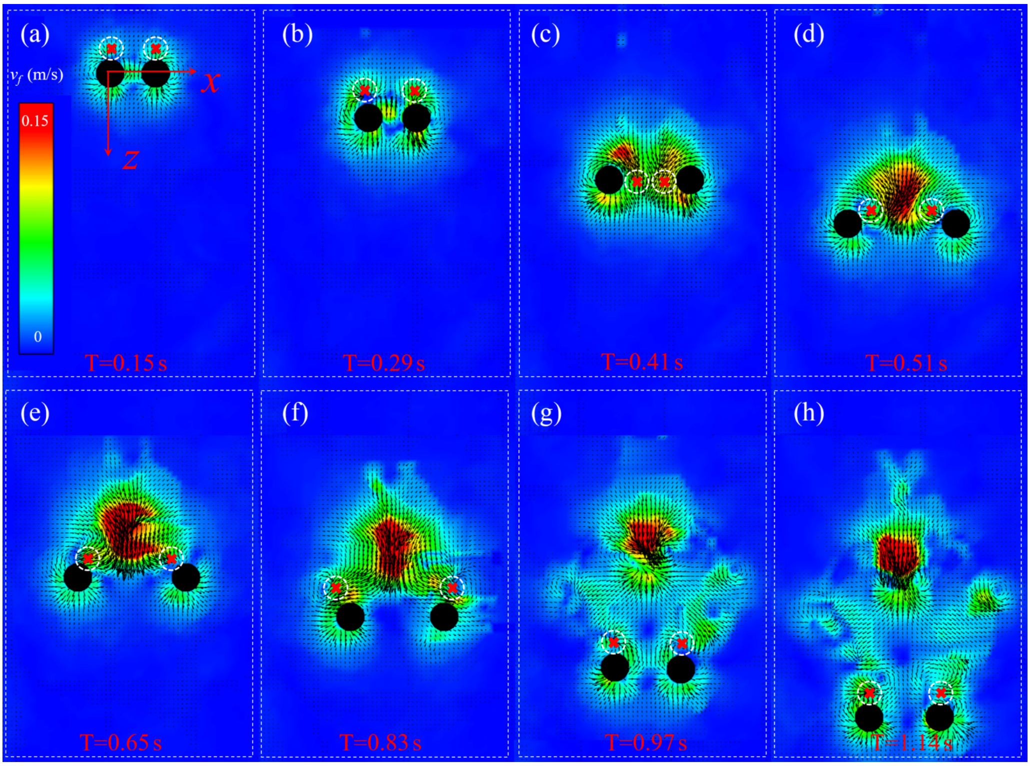

FIG. 11. Contours and vectors of the fluid velocity v_f around twin particles with a size of 40 mm measured using PIV at different instants.

those of small particles. Larger particles correspond to higher Re_p. On the y-z plane, as particle size increases, the mean velocity $\bar{U}_y^*$ becomes even less discernible.

The error bars associated with the velocity curves are more clearly presented in Fig. 10, in terms of standard deviations. Colored curves represent twin particles with different initial gaps, while solid and dashed black lines correspond to individual particles on the x-z or y-z and the x'-z or y'-z planes, respectively. The initial gap has little influence on particle fluctuation velocities in both x and y directions. Larger particles exhibit lower fluctuation velocity intensities. Because of the random deflection of individual particles, their fluctuation velocities are significantly greater than those of twin particles on the x-z and y-z planes. On the deflection plane, the standard deviation of deflection velocity for individual particles, $\sigma(U_{x'}^*)$, is slightly larger than that of twin particles, $\sigma(U_x^*)$, showing that the fluctuation deflection velocity is suppressed due to a mutually supporting effect. On the fluctuation plane, $\sigma(U_{y'}^*)$ and $\sigma(U_y^*)$ are almost identical.

3. Possible reason for the MSP

PIV measurements were employed to visualize the flow field around 40-mm twin settling particles. As shown in Fig. 11, the flow field remained highly symmetrical at different instants during the settling process. In this figure, the x direction denotes the particle deflection direction, and the z direction denotes the falling direction. During the initial stage of settling, the flow structure around the twin particles closely resembles that of an individual particle. The velocity vectors originate from the bottom surfaces of the particles, flow along both sides, and converge near the centers of their top surfaces, as shown in Fig. 11(a). The upward flows between the two particles overlap in this region, producing a locally higher velocity than that outside the particles and, consequently, a lower pressure between them. This pressure difference drives the particles slightly toward each other, as illustrated in Fig. 11(b). Meanwhile, the convergence point of the velocity vectors shifts inward, further amplifying the pressure imbalance. As a result, the internal flow between the particles rapidly transitions from an upward (bottom-to-top) motion to a downward (top-to-bottom) motion, pushing the particles apart, as depicted in Fig. 11(c).

After the twin particles are pushed outward, the flow field in the region between them is no longer constrained by particle boundaries and develops into two vortices, characterized by a downward flow at the center and upward motion along the sides, as shown in Figs. 11(d) and 11(e). As the particles continue to settle, they gradually move away from this vortex region, and new flow patterns are reestablished around each particle. The velocity vectors once again originate from the bottom surfaces and converge at the top, but the convergence points, influenced by the previously shed vortex, now deviate outward, pushing the particles back toward each other, with the corresponding flow field evolution depicted in Figs. 11(f)–11(h).

Throughout the settling process, the convergence points alternately deviate inward and outward, with each deviation driving the particles in the opposite direction. Since the initial deviations of convergence points occur inward, the particles first move apart. Subsequent deviations, influenced by the previously shed vortices, occur in the opposite direction, causing the particles to move in reverse. This mechanism explains why random deflection is strongly suppressed during the settling of twin particles. The twin particles exhibit highly symmetrical motion confined to the initial release plane, characterized by a periodic separation-approach cycle.

C. Settling process of multiple particles

Figure 4(c) presents the partial 3D settling trajectories of triple particles with a size of 40 mm. The settling process of outermost particles is similar to that of the twin particles, showing a typical MSP, while the middle particle randomly deflects during the settling, similar to that of individual particles.

1. Settling trajectories and velocities of three particles

The mean dimensionless settling trajectories and velocities of three 40-mm particles with different initial gaps are shown in Fig. 12. The upper part of the figure depicts the mean trajectories and velocities of outermost particles (labeled "L" and "R") on the x-z and y-z planes, while the lower part shows the mean trajectories and velocities of the middle particle (labeled "M") and individual particles on the x'-z and y'-z planes.

On the x-z plane, the movements of particles L and R show obvious symmetry. After an initial vertical descent, they separate, with their trajectories deflecting laterally until reaching a maximum separation, after which they gradually approach each other. The smaller the initial gap between particles L and R, the faster the cycle. On the y-z plane, the mean particle trajectories almost coincide with the z axis, indicating that the mean fluctuation displacement $\bar{y}^*$ of particles L and R along the trajectory is almost zero. The curves of $\bar{U}_x^*$ for particles L and R are mirror images. After a slight increase and decrease, the mean deflection velocity $\bar{U}_x^*$ presents a sinusoidal curve with decreasing amplitude. Throughout the settling process, the mean fluctuation velocities $\bar{U}_y^*$ of particles L and R are difficult to observe. The mean vertical velocities $\bar{U}_z^*$ of particles L and R are almost coincident. After a sharp increase, a "squat" occurs, and then the vertical velocities $\bar{U}_z^*$ recover to a value slightly less than the peak and fluctuate around it. The smaller the initial gap, the faster the changes in vertical and deflection velocities along the trajectory. Overall, the settling behaviors of particles L and R are almost the same as those of twin particles, showing a typical MSP.

The mean settling trajectories and velocities of the particle M highly coincide with those of individual particles. The presence of particles L and R has almost no effect on the settling process of particle M. On the deflection plane x'-z, after a period of nearly vertical settling, particle M begins to deviate from the vertical trajectory and moves in the opposite direction after reaching the maximum deviation point. On the fluctuation plane y'-z, the mean fluctuation displacements $\bar{y}'^*$

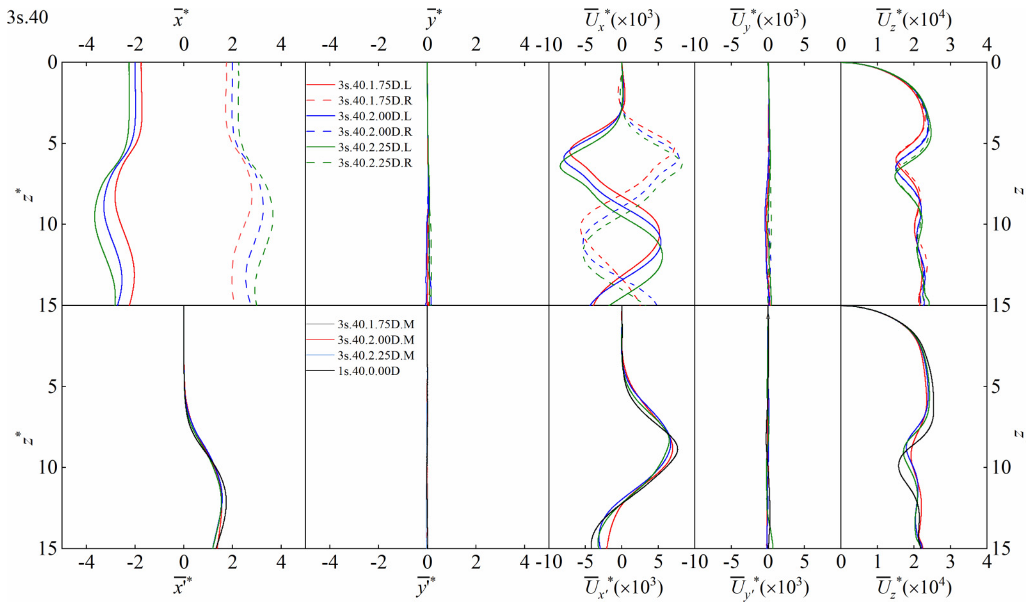

FIG. 12. Mean settling trajectory and velocity of individual and triplet particle configurations with a size of 40 mm on the deflection and fluctuation planes.

are almost zero along the trajectory. In the initial stage, the mean vertical velocity $\bar{U}_z^*$ of particle M increases sharply, and the mean deflection velocity $\bar{U}_x^*$ is almost zero. When the mean vertical velocity $\bar{U}_z^*$ reaches a plateau, the mean deflection velocity $\bar{U}_x^*$ gradually increases in the deflection direction. After the mean vertical velocity $\bar{U}_z^*$ "squats," the mean deflection velocity $\bar{U}_x^*$ reaches a peak value and then increases in the opposite direction after decreasing to zero. During the entire settling process, the mean fluctuation velocity $\bar{U}_{y'}^*$ slightly fluctuates around zero. The initial gap has little effect on the settling process of particle M.

The comparison of standard deviations $\sigma(x^*)$, $\sigma(y^*)$, $\sigma(U_x^*)$, and $\sigma(U_y^*)$ between the triplet particle configuration and the individual particles is shown in Fig. 13, further confirming the above conclusion. That is, the settling behaviors of particles L and R are almost the same as those of twin particles, and particle M exhibits identical settling characteristics to individual particles.

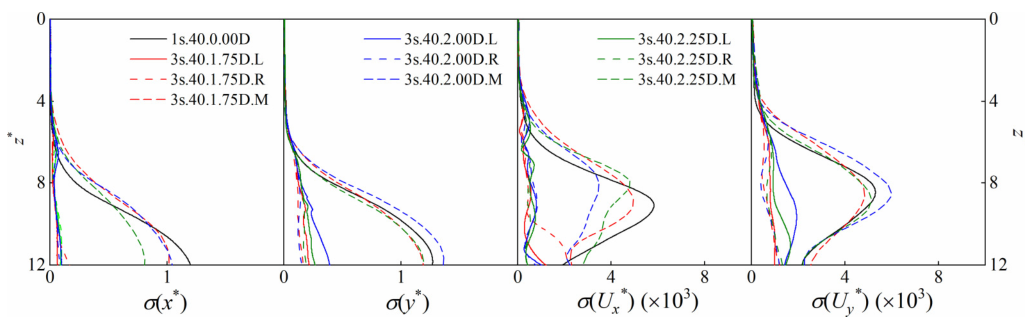

FIG. 13. Standard deviations of displacement and velocity of individual and triple settling particles with a size of 40 mm on the x-z and y-z planes.

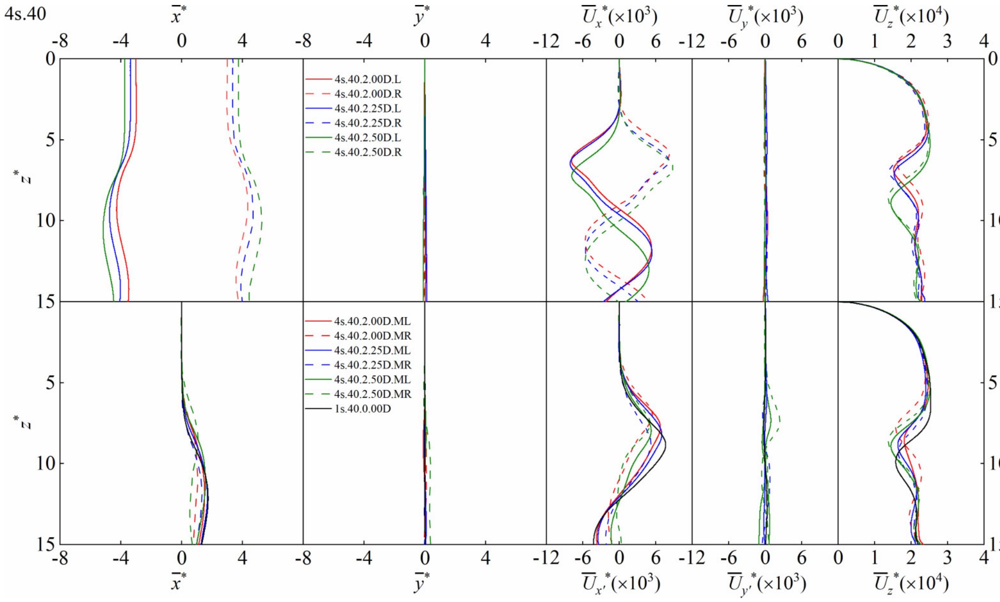

FIG. 14. Mean settling trajectories and velocities of quadruplet particle configuration with a size of 40 mm on the deflection and fluctuation planes.

2. Settling trajectories and velocities of four particles

The mean dimensionless settling trajectories and velocities of quadruplet 40-mm particles with different initial gaps are shown in Fig. 14. The upper part of the figure depicts the mean trajectories and velocities of outermost particles (labeled “L” and “R”) on the x-z and y-z planes, while the lower part shows the mean trajectories and velocities of the middle two particles (labeled “ML” and “MR”) and individual particles on the x'-z and y'-z planes. Like particles L and R of the triple particle configuration, the settling behaviors of particles L and R of the quadruplet particle configuration are highly consistent with those of twin particles, showing a typical MSP.

During the multiparticle settling process, the motion of the middle particle has little influence on the settling behavior of the outermost particles, even when the deflection plane of the middle particle (x'-z plane) coincides with the release plane (x-z plane). The experimental results show that the outermost particles begin to deflect at a smaller falling height than the middle particle. By the time the middle particle starts to deflect, the outermost particles have already moved outward by a considerable lateral distance, forming a clear separation from the middle particle. Consequently, the subsequent deflection of the middle particle does not produce a significant disturbance to the motion of the outermost particles.

The mean trajectories and mean velocity curves of particles ML and MR do not completely coincide with those of individual particles. Although particles ML and MR exhibit some settling characteristics of individual particles, their mean trajectories and mean settling velocities on the deflection and fluctuation planes are more irregular. Different from particle M of the triplet particle configuration, the existence of surrounding particles affects the settling process of particles ML and MR to a certain extent, resulting in their settling behaviors being slightly different from those of individual particles.

3. MSP in the settling process of multiple particles

For multiple settling particles released side by side, the two outermost particles exhibit a typical MSP. The middle particle of the triplet particle configuration randomly deflects during the settling process, similar to the settling behavior of individual particles. However, the middle two particles of the quadruplet particle configuration are affected by surrounding particles and only partially exhibit the settling characteristics of individual particles.

For twin settling particles, the convergence points of the velocity vectors alternately deviate inward and outward, causing the twin particles to move symmetrically within the initial release plane and suppressing random deflection. The mechanism of the MSP can be further inferred from the behavior of the outermost particles in triple and quadruplet configurations. In these cases, each outermost particle interacts only with its neighboring particle on one side. During the initial stage of settling, the convergence point of the velocity vectors on the top of the outermost particle shifts toward its neighboring particle, thereby pushing it away. As settling continues, the convergence point alternates between directions toward and away from the neighboring particle, leading to a periodic back-and-forth deflection of the outermost particle. In other words, the two outermost particles do not affect each other directly; the MSP arises because the initial deflection of each outermost particle is governed by the presence of its neighboring particle on one side.

However, the middle particle of the triple particle configuration is equally affected by the neighboring particles on both sides. These two influences counterbalance each other, making the settling behavior of the middle particle consistent with that of individual particles. In contrast, for the quadruplet particle configuration, each of the two middle particles has one neighboring particle on one side and two on the other. The asymmetric influences from both sides cannot be completely offset, preventing these middle particles from exhibiting the dynamic characteristics typical of a canonical twin-particle system. Instead, their behavior more closely resembles the random deflection observed during the settling of individual particles, although their overall settling process is distinct from that of individual particles. More precise PIV measurements are required in future work to verify these inferences.

IV. CONCLUSIONS

This study experimentally investigates the 3D settling process of centimeter-sized spherical particles in still water using CBV and PIV techniques. The main conclusions are summarized as follows.

During the settling process, an individual particle undergoes random deflection in all directions with approximately equal probability. The 3D settling trajectory can be decomposed into the deflection and fluctuation planes. On the deflection plane, after a period of nearly vertical settling, the particle begins to deflect toward the maximum deviation point, and then moves in the opposite direction after reaching it. On the fluctuation plane, the particle fluctuates around the z axis. The mean deflection velocity presents a quasisinusoidal curve after a slight increase and decrease, and the mean vertical velocity increases sharply and stabilizes at a value slightly lower than the peak after a “squat.” The mean fluctuation velocity remains almost zero during the entire settling process.

Twin particles exhibit a typical MSP during the settling process. They move in an almost synchronized and mirror-image fashion, with their trajectories featuring lateral outward deflection to a maximum after an approximately vertical segment, and then gradually approaching each other. The deflection planes of twin particles are constrained to the initial release plane. The mean settling trajectories and velocities of twin particles are similar to those of individual particles. The deflection and subsequent return motion of each particle results in a cycle of separation and approach. The smaller the initial gap at release, the faster the separation-approach cycle proceeds. Furthermore, the smaller the particles, the more fully developed the particle settling process.

PIV observations show that, for an individual particle, the convergence point of the velocity vectors on the particle’s top surface randomly shifts during settling, pushing the particle in the opposite direction. The vortex generated near the displaced convergence point subsequently induces the next convergence point on the opposite side, driving the particle back. The random initial deviation of the convergence point leads to random deflection, while the subsequent alternating

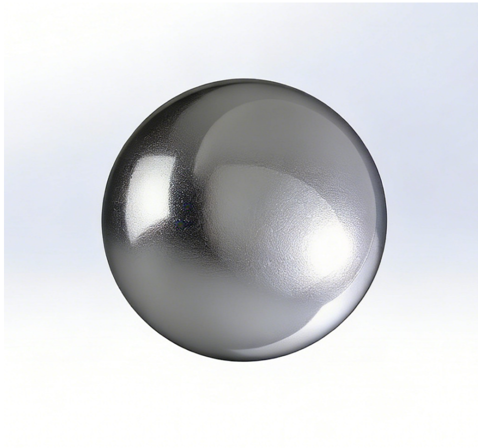

FIG. 15. 3D-printed custom hollow particle.

formation of convergence points causes the particle to oscillate back and forth approximately within the same plane during settling.

For twin particles released side by side, the initial convergence point of the velocity vectors consistently shifts toward the inner region between the two particles, thereby suppressing random deflection. The subsequent evolution of the convergence points resembles that of an individual particle, resulting in the twin particles settling nearly within the same plane and exhibiting periodic separation-approach motion.

The MSP is also observed during the settling of multiple spherical particles released side by side. The two outermost particles display pronounced mutual support, with their deflection direction restricted by flow field disturbances caused by particles on one side. In contrast, the middle particle of the triplet particle configuration shows significant random deflection, resembling the behavior of individual settling particles. The effects of other particles on both sides of the middle two particles of the quadruplet particle configuration cannot fully offset each other, resulting in a more complicated settling process.

This experimental research highlights the strong randomness inherent in the settling behavior of individual particles and the effective suppression of random deflection through the MSP in twin particles and the outermost particles of multi-particle configurations. These findings provide a robust experimental basis for validating and improving current computational fluid dynamics methods. Future work requires more sophisticated PIV experiments to explore the inducing mechanism of particle random deflection and the action mechanism of the MSP.

It should be noted that the present study did not quantify the potential rotation of particles during the settling process. Although the release method was designed to minimize initial disturbances, particle rotation induced by wake interactions or slight asymmetries was not measured. Future work incorporating rotational tracking is necessary to fully understand its influence on particle trajectories and velocities.

ACKNOWLEDGMENTS

Financial support from the Fundamental Research Funds for the Central Universities (Grant No. 202462001) and the National Natural Science Foundation of China (Grant No. 52171280) is gratefully acknowledged.

DATA AVAILABILITY

The data that support the findings of this article are openly available.

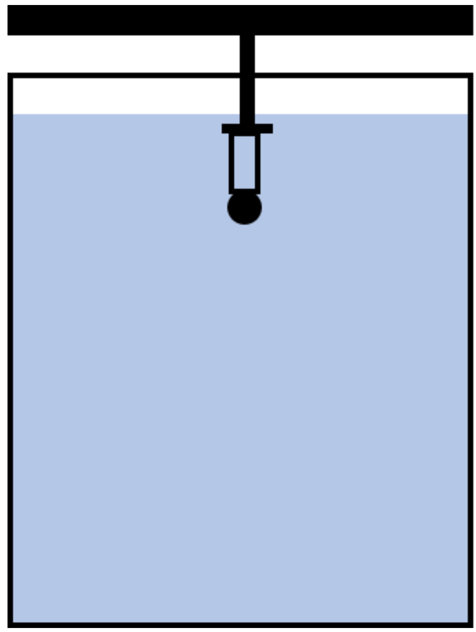

FIG. 16. Modified release device.

APPENDIX

To systematically investigate the influence of thin threads during the settling process of test particles, this study designed and conducted a refined comparative test. The custom 40-mm-diam particle used was a hollow spherical shell, fabricated via 3D printing using iron with a density of 7800 ± 0.5 kg/m^3, as shown in Fig. 15. By creating an internal cavity with a radius of 9.13 mm, the overall density of the custom particle was precisely adjusted to 1254.3 kg/m^3, ensuring consistency with the density of the test particle to guarantee the accuracy of the experiment.

The experimental devices were modified based on the original setup shown in Fig. 1. In the modified configuration, an electromagnet with a demagnetization function was submerged in the water to hold the custom particle, as shown in Fig. 16. Apart from this adjustment to the electromagnet's placement, all other components of the setup were identical to those in experiment I to

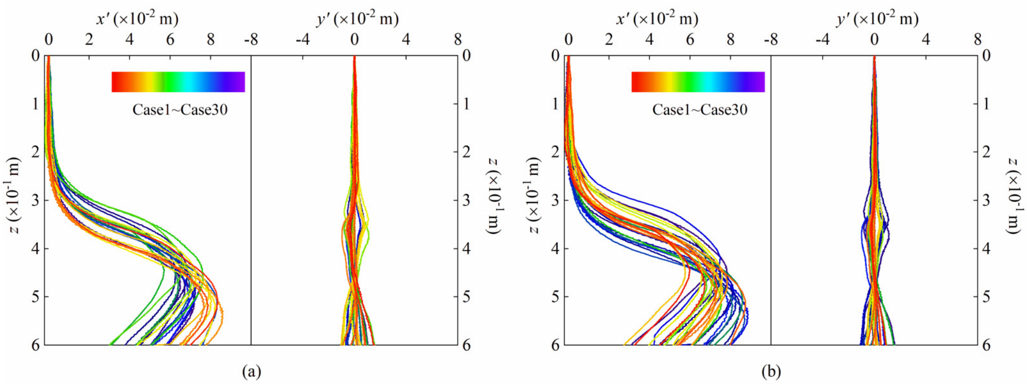

FIG. 17. Trajectories from 30 repeated experiments on the deflection and fluctuation planes: (a) electromagnetic release and (b) thin-thread release.

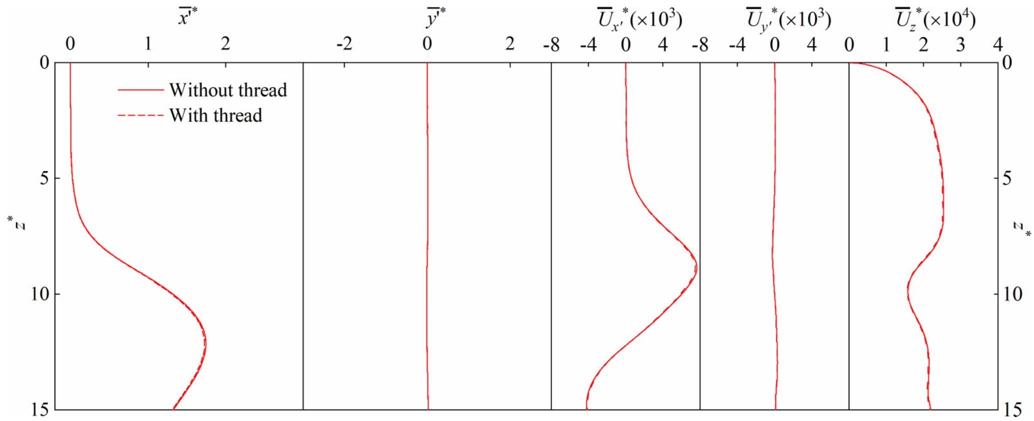

FIG. 18. Mean settling trajectories and velocities of 40-mm individual particles on deflection and fluctuation planes under electromagnetic release and thin-thread release.

eliminate interference from extraneous variables. During the experiment, the custom particle was firmly attached to the bottom of the electromagnet when the power was on. Upon disconnection of the power supply, the electromagnet demagnetized, and the particle instantaneously began to settle freely in the quiescent water.

Figure 17(a) shows the trajectories of custom 40-mm particles released at the center of the water tank from 30 repeated experiments on the deflection plane and fluctuation plane under electromagnetic release. The 30 trajectories exhibit similar characteristics: on the deflection plane, after an approximately vertical settling stage, the particles move toward the maximum deflection point and then reverse their motion direction; on the fluctuation plane, the particles fluctuate around the z axis. These features are highly consistent with those in Fig. 17(b) for particles released at the center of the water tank using the thin-thread method. Figure 18 presents the mean dimensionless trajectories and velocities for 40-mm individual particles released at the center of the water tank by electromagnetic adsorption and thin-thread connection on deflection and fluctuation planes. The solid red lines represent the electromagnetic release case, and the dashed red lines correspond to the thin-thread release case. The two red curves show excellent agreement in both trajectories and velocities, indicating that the influence of the thin thread during the settling process of particles is negligible.

[1] J. L. Deng, X. M. Wang, H. Y. Wang, H. D. Cao, and J. X. Xia, Quantitative description of size and mass distribution of polymetallic nodules in northwest Pacific Ocean basin, Minerals **14**, 1230 (2004).

[2] T. Kuhn and C. Rühlemann, Exploration of polymetallic nodules and resource assessment: A case study from the German contract area in the Clarion-Clipperton zone of the tropical northeast Pacific, Minerals **11**, 618 (2021).

[3] R. Kurose and S. Komori, Drag and lift forces on a rotating sphere in a linear shear flow, J. Fluid Mech. **384**, 183 (1999).

[4] P. P. Brown and D. F. Lawler, Sphere drag and settling velocity revisited, J. Environ. Eng. **129**, 222 (2003).

[5] Q. Zhou and N. S. Cheng, Experimental investigation of single particle settling in turbulence generated by oscillating grid, Chem. Eng. J. **149**, 289 (2009).

[6] G. H. Good, P. J. Ireland, G. P. Bewley, E. Bodenschatz, L. R. Collins, and Z. Warhaft, Settling regimes of inertial particles in isotropic turbulence, J. Fluid Mech. **759**, R3 (2014).

[7] S. Shahi and E. Kuru, Experimental investigation of the settling velocity of spherical particles in power-law fluids using particle image shadowgraph technique, Int. J. Miner. Process. **153**, 60 (2016).
[8] J. Feng, H. H. Hu, and D. D. Joseph, Direct simulation of initial value problems for the motion of solid bodies in a Newtonian fluid Part 1. Sedimentation, J. Fluid Mech. **261**, 95 (1994).
[9] G. Gheissary and B. H. A. A. van den Brule, Unexpected phenomena observed in particle settling in non-Newtonian media, J. Non-Newton. Fluid Mech. **67**, 1 (1996).
[10] M. Jenny, J. Dušek, and G. Bouchet, Instabilities and transition of a sphere falling or ascending freely in a Newtonian fluid, J. Fluid Mech. **508**, 201 (2004).
[11] C. H. J. Veldhuis and A. Biesheuvel, An experimental study of the regimes of motion of spheres falling or ascending freely in a Newtonian fluid, Int. J. Multiphase Flow **33**, 1074 (2007).
[12] M. Horowitz and C. H. K. Williamson, The effect of Reynolds number on the dynamics and wakes of freely rising and falling spheres, J. Fluid Mech. **651**, 251 (2010).
[13] A. F. Fortes, D. D. Joseph, and T. S. Lundgren, Nonlinear mechanics of fluidization of beds of spherical particles, J. Fluid Mech. **177**, 467 (1987).
[14] A. Doostmohammadi and A. M. Ardekani, Interaction between a pair of particles settling in a stratified fluid, Phys. Rev. E **88**, 023029 (2013).
[15] S. M. Dash and T. S. Lee, Two spheres sedimentation dynamics in a viscous liquid column, Comput. Fluids **123**, 218 (2015).
[16] C. C. Liao, W. W. Hsiao, T. Y. Lin, and C. A. Lin, Simulations of two sedimenting-interacting spheres with different sizes and initial configurations using immersed boundary method, Comput. Mech. **55**, 1191 (2015).
[17] L. H. Tsai, C. C. Chang, T. W. Pan, and R. Glowinski, Numerical study of the wall effect on particle sedimentation, Int. J. Comput. Fluid Dyn. **32**, 158 (2018).
[18] D. D. Joseph, Y. J. Liu, M. Poletto, and J. Feng, Aggregation and dispersion of spheres falling in viscoelastic liquids, J. Non-Newton. Fluid Mech. **54**, 45 (1994).
[19] J. Wu and R. Manasseh, Dynamics of dual-particles settling under gravity, Int. J. Multiph. Flow. **24**, 1343 (1998).
[20] C. Cao, S. Chen, J. Li, Z. Liu, L. Zha, S. Bao, and C. Zheng, Simulating the interactions of two freely settling spherical particles in Newtonian fluid using lattice-Boltzmann method, Appl. Math. Comput. **250**, 533 (2015).
[21] D. Nie and J. Lin, Simulation of sedimentation of two spheres with different densities in a square tube, J. Fluid Mech. **896**, A12 (2020).
[22] C. R. Chu, T. R. Wu, Y. F. Tu, S. K. Hu, and C. L. Chiu, Interaction of two free-falling spheres in water, Phys. Fluids **32**, 033304 (2020).
[23] J. Liu, P. Zhang, Y. Xiao, Z. Wang, S. Yuan, and H. Tang, Interaction between dual spherical particles during settling in fluid, Phys. Fluids **33**, 013312 (2021).
[24] C. L. Chiu, C. M. Fan, and C. R. Chu, Numerical analysis of two spheres falling side by side, Phys. Fluids **34**, 072112 (2022).
[25] Y. Xiao, J. Liu, P. Zhang, J. Zhou, D. Liang, Z. Wang, T. Zhang, S. Yuan, and H. Tang, Experimental study of the settling of twin spherical particles released side by side: The impact of particle size, fluid viscosity, initial spacing, and particle density, Int. J. Sediment Res. **38**, 83 (2023).
[26] R. Di Felice, The sedimentation velocity of dilute suspensions of nearly monosized spheres, Int. J. Multiphase Flow **25**, 559 (1999).
[27] W. B. Daniel, R. E. Ecke, G. Subramanian, and D. L. Koch, Clusters of sedimenting high-Reynolds-number particles, J. Fluid Mech. **625**, 371 (2009).
[28] Y. J. Chou, S. H. Gu, and Y. C. Shao, An Euler-Lagrange model for simulating fine particle suspension in liquid flows, J. Comput. Phys. **299**, 955 (2015).
[29] S. Shahi and E. Kuru, An experimental investigation of settling velocity of natural sands in water using particle image shadowgraph, Powder Technol. **281**, 184 (2015).
[30] N. Zhang, W. Zhu, H. He, Y. Lv, and S. Wang, Experimental study on settling velocity of soil particles in dredged slurry, Mar. Geores. Geotechnol. **35**, 747 (2017).

[31] A. J. Petersen, L. Baker, and F. Coletti, Experimental study of inertial particles clustering and settling in homogeneous turbulence, J. Fluid Mech. **864**, 925 (2019).

[32] N. A. Patankar, P. Singh, D. D. Joseph, R. Glowinski, and T. W. Pan, A new formulation of the distributed Lagrange multiplier/fictitious domain method for particulate flows, Int. J. Multiphase Flow **26**, 1509 (2000).

[33] Z. G. Feng and E. E. Michaelides, The immersed boundary-lattice Boltzmann method for solving fluid–particles interaction problems, J. Comput. Phys. **195**, 602 (2004).

[34] A. E. Yacoubi, S. Xu, and Z. J. Wang, Computational study of the interaction of freely moving particles at intermediate Reynolds numbers, J. Fluid Mech. **705**, 134 (2012).

[35] D. Nie, J. Lin, and M. Zheng, Direct numerical simulation of multiple particles sedimentation at an intermediate Reynolds number, Commun. Comput. Phys. **16**, 675 (2014).

[36] L. Sun, R. Zhang, Z. W. Zhou, J. F. Yin, and D. D. Meringolo, Influences of particle-particle and particle-wall interactions on the settling behaviors of the centimeter-sized spherical particles, Eur. J. Mech. B. Fluids **115**, 204387 (2026).

[37] Z. Y. Zhang, A flexible new technique for camera calibration, IEEE Trans. Pattern Anal. Mach. Intell. **22**, 1330 (2000).